Unraveling the Performance Descriptors for Designing Single-Atom Catalysts on Defective MXenes for Exclusive Nitrate-To-Ammonia Electrocatalytic Upcycling

Xutao Gao and Edmund C. M. Tse*

Electrocatalytic nitrate reduction reaction (NO_3RR) is a promising approach for converting nitrate into environmentally benign or even value-added products such as ammonia (NH_3) using renewable electricity. However, the poor understanding of the catalytic mechanism on metal-based surface catalysts hinders the development of high-performance NO_3RR catalysts. In this study, the NO_3RR mechanism of single-atom catalysts (SACs) is systematically explored by constructing single transition metal atoms supported on MXene with oxygen vacancies (O_v-MXene) using density functional theory (DFT) calculations. The results indicate that Ag/O_v-MXene (for precious metal) and Cu/O_v-MXene (for non-precious metal) are highly efficient SACs for NO_3RR toward NH_3, with low limiting potentials of -0.24 and -0.34 V, respectively. Furthermore, these catalysts show excellent selectivity toward ammonia due to the high energy barriers associated to the formation of byproducts such as NO_2, NO, N_2O, and N_2 on Ag/O_v-MXene and Cu/O_v-MXene, effectively suppressing the competitive hydrogen evolution reaction (HER). The findings not only offer new strategies for promoting NH_3 production by MXene-based SACs electrocatalysts under ambient conditions but also provide insights for the development of next-generation NO_3RR electrocatalysts.

1. Introduction

Nitrate (NO_3^-) pollution has become a serious human-caused issue affecting aquatic ecosystems and drinking water resources due to the release of NO or NO_2 from nitrogen-containing fuels, the emission of NOx-containing fertilizers into soil and groundwater, and the discharge of nitrate-containing industrial wastewater.[1,2] The accumulation of nitrate poses a significant threat to the environment and human health, including cancer and blue baby syndrome.[3] Therefore, it is imperative to remove excess nitrate ions from contaminated water to complete the artificial nitrogen cycle. To address this challenge, various technologies, such as reverse osmosis,[4] ion exchange,[5] and bacterial denitrification,[6] have been developed. However, these technologies have considerable drawbacks such as prohibitively high post-treatment costs, strict reaction conditions, and complex multi-stage processes. Recent reports showed that electrocatalytic NO_3RR is an alternative method for converting nitrate into harmless products and value-added products using renewable electricity.[7] Compared to the traditional approaches, NO_3RR does not require additional reducing agents to convert NO_3^- into products like NH_3, N_2, NO, NO_2, N_2O, and NH_2OH, as electrons are used for nitrate reduction.[8] NH_3 is a desired product that can be generated from NO_3^- via the transfer of nine protons and eight electrons ($NO_3^- + 9H^+ + 8e^- \rightarrow NH_3 + 3H_2O$ $E^0 = 0.82$ V). Though this low-temperature ammonia synthesis method is promising, developing catalysts with high activity and selectivity toward ammonia under ambient conditions remains a challenge due to the sluggish reaction kinetics and competitive HER.

Significant research efforts have been dedicated to developing electrocatalysts with high activity, selectivity, and durability for the reduction of NO_3^- into NH_3 to mitigate nitrate pollution.[9] Previous studies have investigated the mechanism, activity, and selectivity on transition metal (TM) electrocatalysts for NO_3RR, where the rate-determining step (RDS) is deduced to be the reduction of nitrate into nitrite (NO_2^-) on the catalyst surface in acidic condition based on the Tafel slope observed.[10–12] Platinum group metals (PGMs) and coinage metals have shown NO_3RR activities under acidic conditions and potentials ranging from 0 to 0.4 V versus RHE, with the activities of Rh > Ru > Ir > Pd ≈ Pt and Cu > Ag > Au, respectively.[10] Although pure Rh and Cu metal catalysts display relatively high NO_3RR activities, they do not readily display high stability, activity, and selectivity toward NH_3 under other

X. Gao, E. C. M. Tse
Department of Chemistry
HKU-CAS Joint Laboratory on New Materials
University of Hong Kong
Hong Kong SAR China
E-mail: ecmtse@hku.hk

ADVANCED
SCIENCE NEWS
www.advancedsciencenews.com

NANO · MICRO
small
www.small-journal.com

reaction conditions. To overcome these limitations, multicomponent electrocatalysts have been developed, where adjusting the ratio of transition metals in alloy catalysts can significantly enhance NO_3RR performance compared to their pure metal counterparts. For example, a stable CuNi alloy electrocatalyst displayed a higher NO_3RR performance than pure Ni and Cu metals.[13] Besides transition metal-based electrocatalysts, other metal oxides, such as TiO_2 enriched with oxygen vacancies as well as CuO nanowire arrays, have also exhibited high NO_3RR performance with remarkable Faraday efficiency and selectivity toward ammonia.[14–16]

The development of nitrate electrocatalysts for NO_3RR has posed a significant challenge due to the lack of a clear understanding of the catalytic mechanism on metal active sites, despite numerous transition metal-based electrocatalysts having been developed. Recently, SACs have drawn extensive attention in the heterogeneous catalysis community.[17–21] Owing to the maximal utilization of active sites, SACs hold the promise to possess high activity and selectivity in catalytic reactions such as CO oxidation,[22] HER,[23] oxygen reduction reaction (ORR),[24] oxygen evolution reaction (OER),[25] CO_2 reduction reaction (CO_2RR),[26] nitrogen reduction reaction (N_2RR),[27–30] CO_2 and N_2 coupling reactions,[31] and nitrate reduction reaction (NO_3RR).[32,33]

MXenes are a unique family of 2D layered materials that exhibit excellent conductivity and chemical stability.[34–36] Recently, MXenes have been applied as electrocatalysts for HER,[37,38] N_2RR,[39–42] and CO_2RR.[43–45] However, the basal plane of the MXene is readily functionalized by O^{2-}, OH^-, or F^- groups, resulting in no exposed metal sites on the surface of MXene. Therefore, MXenes cannot efficiently catalyze more complex reactions that involve multiple proton-coupled electron transfer (PCET) steps.[46] Recently, the engineering of vacancies has emerged as a promising strategy to stabilize SACs on MXene materials and enhance their electrocatalytic performance.[28] Zhang et al. synthesized $Mo_2TiC_2T_x$ MXene nanosheets with Mo vacancies serving as the anchoring sites for single Pt atoms ($Mo_2TiC_2T_x$-Pt_{SA}). The synthesized catalysts showed high durability and outstanding hydrogen evolution reaction activity.[47] Chen and co-workers developed a Ti-deficit 2D MXenes nanosheet and anchored Pt single atoms onto the sites previously occupied by Ti. The as-synthesized Pt-based SAC, $Pt_1/Ti_{3-x}C_2T_y$, exhibited efficient conversion of aniline into amide.[48]

Utilizing first-principles calculations, the feasibility of utilizing single transition metal atoms embedded on defective MXenes nanosheets, namely $Ti_{3-x}C_2O_y$ with a Ti vacancy and $Mo_{2-x}TiC_2O_2$ with a Mo vacancy, for N_2RR has been systematically explored. The results indicate that $W/Ti_{3-x}C_2O_y$ and $Mo_{2-x}TiC_2O_2$-Zr_{SA} showed the lowest potential-determining step (PDS) barrier (0.11 and 0.15 eV) while suppressing competitive HER.[28,49] However, to the best of our knowledge, the use of SACs supported on defective MXenes nanosheets for NO_3RR toward NH_3 has not been reported.

In this study, we chose the most extensively studied $Ti_3C_2O_2$ MXene as a representative substrate to construct SACs. Ti_3C_2 was the first reported type of MXene in 2011 and was the most studied for its availability, tunable modification, and unique electronic properties with applications in the fields of photocatalysis,

energy conversion and storage, and electronic devices.[50] Here, linear scaling plot and contour plot are established to explain activity trends on TM/O_v-MXene as well as to identify the metal/O_v-MXene hybrid materials with the most efficient NO_3RR activity as well as the highest selectivity toward NH_3 by suppressing competitive HER.

2. Results and Discussion

2.1. Screening NO_3^- Adsorption on SACs

First, 3d-, 4d- and 5d- transition metal (TM) atoms are embedded into the MXene support ($Ti_{3-x}C_2T_y$). The NO_3RR performance of SACs is then comprehensively investigated using first-principles calculations for 22 transition metals. Density functional theory calculations are performed to calculate the density of state (DOS) of the pure $Ti_3C_2O_2$ MXene structure (Figure S1, Supporting Information). The calculated DOS of the MXene exhibits a conductor-like electronic structure, with a nonzero value around the Fermi level (E_F), and is mainly derived from the Ti 3d, O 2p, and C 2p orbitals, consistent with previous studies.[35] The structure of $TM/Ti_3C_2O_2$ is constructed by removing one O atom from the MXene surface, leading to an O vacancy (O_v), followed by replacing the exposed Ti with different transition metal atoms to form an O vacancy TM-doped MXene (**Figure 1**a). The first step of the NO_3RR process is NO_3^- adsorption, which is critical for the entire catalytic reaction. We investigated the adsorption energies of NO_3^- on bare MXene and O_v-MXene, as shown in Figure S2 (Supporting Information). The adsorption energies are 2.02 and -0.94 eV for bare MXene and O_v-MXene, respectively. The introduction of an O vacancy greatly improves the NO_3^- adsorption energetics. For Ta/O_v-MXene, W/O_v-MXene, and Re/O_v-MXene, the adsorbed NO_3^- decomposes into NO_2 and one O atom. As shown in Figure S3 (Supporting Information), the O atom fills the oxygen vacancy on the O-terminated MXene surface, hindering the further reduction of NO_3^-. Therefore, these catalysts are considered not suitable for NO_3RR and are not further explored. Since competitive HER can disrupt the NO_3RR process, we also investigated the adsorption energies of NO_3^- (ΔG_{*NO3}) and proton (ΔG_{*H}) on TM/O_v-MXene for comparison (Figure 1b), and the corresponding configurations of $^*H$ and $^*NO_3$ are shown in Figure S4 (Supporting Information). Notably, the ΔG_{*NO3} of Cr, Mn, Fe, Ni, Cu, Zr, Nb, Mo, Pd, Ag, Hf, Ta, Re, Au doped O_v-MXene are more negative than ΔG_{*H}, indicating NO_3RR is a more favorable process on these TM/O_v-MXene relative to HER.

The adsorption trends of NO_3^- on TM/O_v-MXene are investigated by probing the relationship between the charge transfer of TM atoms and the adsorption energy of NO_3^- (ΔG_{*NO3}) (Figure 1c). Detailed bond lengths, binding energies, and charge transfers for NO_3^- adsorption on different TM/O_v-MXenes are summarized in Table S1 (Supporting Information). A good correlation coefficient ($R^2 = 0.75$) suggests a linear relationship between charge transfer and ΔG_{*NO3}, further indicating that larger charge transfer of TM atoms results in higher NO_3^- adsorption energy. For instance, Hf/O_v-MXene exhibits the highest adsorption energy of NO_3^- of -1.41 eV with the largest charge transfer of -2.15 e$^-$.

ADVANCED
SCIENCE NEWS
www.advancedsciencenews.com
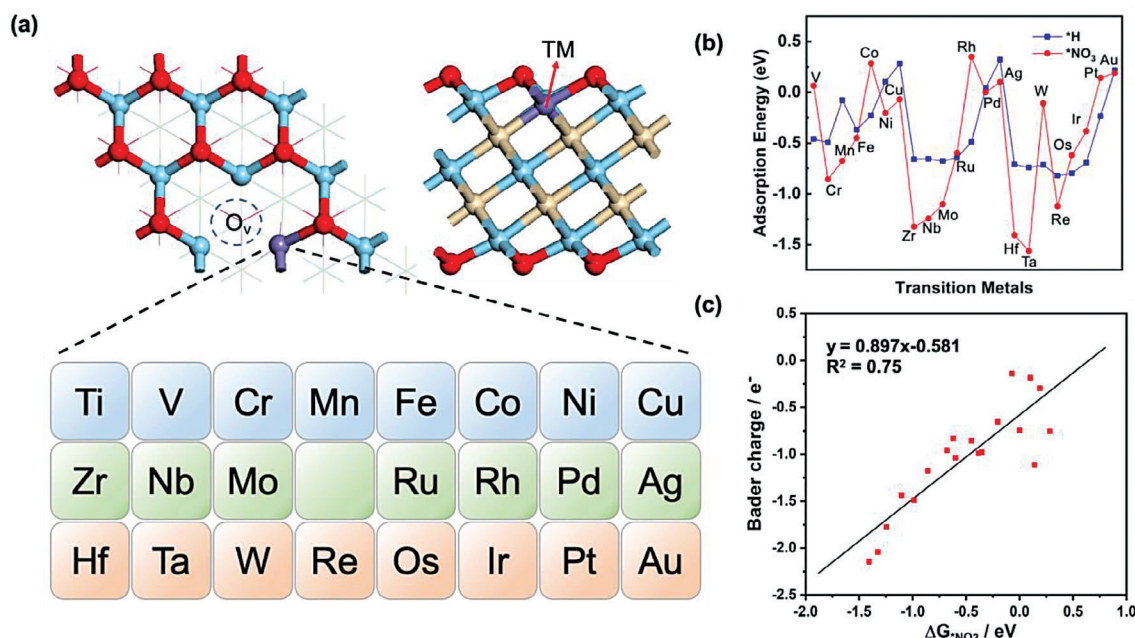
NANO · MICRO
small
www.small-journal.com

Figure 1. a) Top and side views of the atomic structure of TM/O_v-MXene. Atom labels: C (white), Ti (blue), O (red), and TM (purple). The screened TM atoms (from Ti to Au) are listed. b) Comparison of adsorption energies of NO_3^- and H^+ on TM/O_v-MXene. c) The scaling relation between charge transfer of TM atoms and NO_3^- adsorption energies.

2.2. NO₃RR Mechanism on TM/O_v-MXene

Electrochemical conversion of NO_3^- into NH_3 via eight electron transfer steps involves various intermediates and products (e.g., NH_3, NO_2, NO, N_2O, and N_2). It has been reported that NH_3/NH_4^+ is the most thermodynamically stable product under negative potential bias.[51] To understand the NO₃RR mechanism on TM/O_v-MXene, we investigate the proposed reaction pathways with one coupled proton + electron ($H^+ + e^-$) pair involved in each elementary step in line with previous studies.[13,14] The intermediates involved in the reaction pathway on TM/O_v-MXene are optimized by DFT calculation. The NO₃RR performance of TM/O_v-MXene is evaluated by comparing the computed limiting potentials ($U_L = -\Delta G_{max}/e$, where ΔG_{max} is the maximum of the free energy change among all elementary steps). **Figure 2**a shows the proposed reaction pathways and the generated products, while the limiting potentials (U_L) for each TM atom are summarized in Figure 2b. We find that the U_L values become less negative from going from left to right on the periodic table for 3d-, 4d- and 5d- TM atoms. Pt/O_v-MXene displayed the lowest NO₃RR energy barrier to generate NH_3. However, HER is found to outcompete NO₃RR on Pt/O_v-MXene, as shown in Figure 1b, indicating Pt/O_v-MXene is not an ideal catalyst for NO₃RR toward NH_3. The next-best NO₃RR catalyst after Pt/O_v-MXene is Ag/O_v-MXene, which exhibits efficient NO₃RR activity with a limiting potential of −0.24 V. For non-precious TM, Cu/O_v-MXene displays the lowest limiting potential of −0.34 V. These two TM/O_v-MXenes also possess high preference toward NH_3 by suppressing competitive HER, demonstrating that they are promising electrocatalysts for selective NO₃RR.

Taking ΔG_{*NO3} as a descriptor, the scaling relationship between the limiting potential on TM/O_v-MXene and ΔG_{*NO3} is constructed in Figure 2c. Notably, we observe decent R^2 values (0.854 and 0.968), indicating that ΔG_{*NO3} is an excellent descriptor for NO₃RR toward NH_3. In addition, we identified six TM/O_v-MXenes with the lowest limiting potentials (Figure 2c, red circle). Our results further demonstrate that the protonation step of $^*NO_3$ ($^*NO_3 + H^+ + e^- \rightarrow {}^*HNO_3$) serves as the potential-determining step (PDS) for Pt and Pd, whereas for other TMs, the protonation step of $^*NO_2$ ($^*NO_2 + H^+ + e^- \rightarrow {}^*HNO_2$) is the PDS. Based on these findings, we constructed a contour plot of limiting potentials as a function of two PDSs ($^*NO_3 + H^+ + e^- \rightarrow {}^*HNO_3$ and $^*NO_2 + H^+ + e^- \rightarrow {}^*HNO_2$), as shown in Figure 2d. The red and blue colors on the contour plot correspond to low and high limiting potentials, respectively. Our results reveal that Pt, Ag, Pd, Au, Cu, and Ni transition metals on O_v-MXene are located close to the red region on the contour plot, indicating their high activity toward NO₃RR.

2.3. NO₃RR Performance of Ag/O_v-MXene and Cu/O_v-MXene

Based on our computational analysis, Ag/O_v-MXene is determined to be the most efficient electrocatalyst for NO₃RR among the TM/O_v-MXenes while concurrently inhibiting the competitive HER. Additionally, Cu/O_v-MXene has been established as the most competent earth-abundant electrocatalyst for NO₃RR featuring non-precious metals (NPMs). During the NO₃RR process, it is noted that two configurations of $^*NO_2$ (1-O binding mode and 2-O binding mode) are considered for TM/O_v-MXene. The detailed adsorption energies and bond lengths are summarized in Table S2 (Supporting Information). Free energy diagrams for NO₃RR on Ag/O_v-MXene and Cu/O_v-MXene via the 1-O pathway are presented in **Figure 3**a,b, respectively, while those for
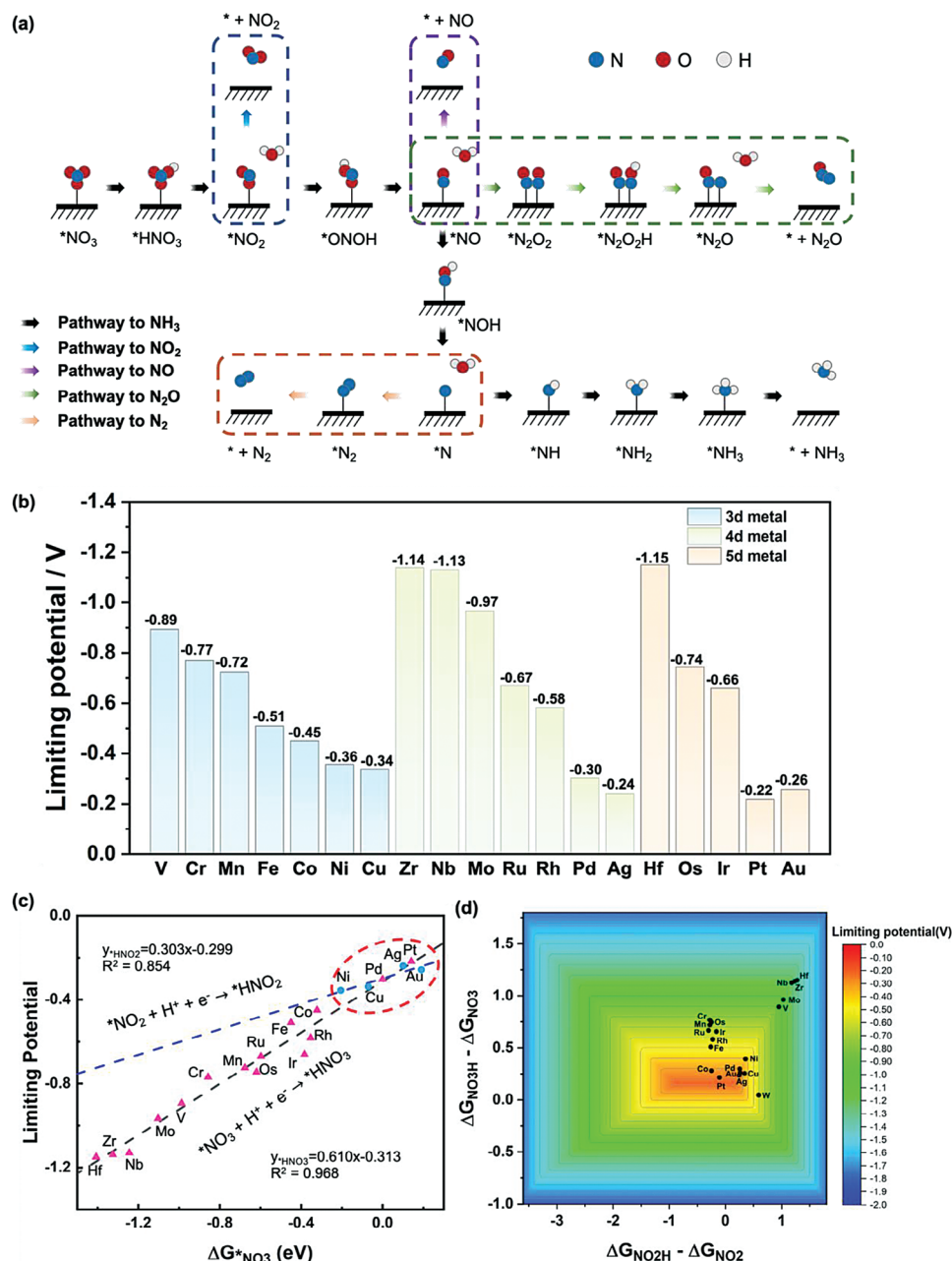
Figure 2. a) Reaction pathways of NO_3RR to NH_3 as well as byproducts including NO_2, NO, N_2O, and N_2. b) Summary of limiting potentials on TM/O_v-MXene for NO_3RR. c) Scaling relationship between the calculated limiting potential of NO_3RR and ΔG_{*NO3}. d) Contour plot of limiting potential as a function of two potential-determining steps ($^*NO_3 + H^+ + e^- \rightarrow {}^*HNO_3$ and $^*NO_2 + H^+ + e^- \rightarrow {}^*HNO_2$).

the 2-O pathway are illustrated in Figures S5 and S6 (Supporting Information). Additionally, the corresponding structures of NO_3RR intermediates for the 1-O pathway and 2-O pathway are displayed in Figure 3c and Figure S7 (Supporting Information), respectively. We observe that the adsorption energy of NO_2 via the 1-O pathway is lower than that of the 2-O pathway on Ag/O_v-MXene and Cu/O_v-MXene. Consequently, the 1-O binding mode pathway is expected to be dominant despite the lower limiting potential of 2-O. For the NO adsorption configurations, $^*ON$ (binding via the O-end) and $^*NO$ (binding via the N-end) binding

modes were considered. The calculated results in Figures S8 and S9 (Supporting Information) show that the $^*NO$ binding modes are -1.06 and -1.08 eV lower in energy than the $^*ON$ binding modes on Ag/O_v-MXene and Cu/O_v-MXene, respectively. These results suggest that $^*NO$ is more thermodynamically favorable than $^*ON$. For the $^*ONOH$ to $^*NO$ process, since $^*ONOH$ binds via the O-end while $^*NO$ binds via the N-end, a switch from $^*ON$ to $^*NO$ is hypothesized. To validate this hypothesis, transition state calculation for $^*ON$-to-$^*NO$ flipping was calculated. As shown in Figures S8 and S9 (Supporting Information), the
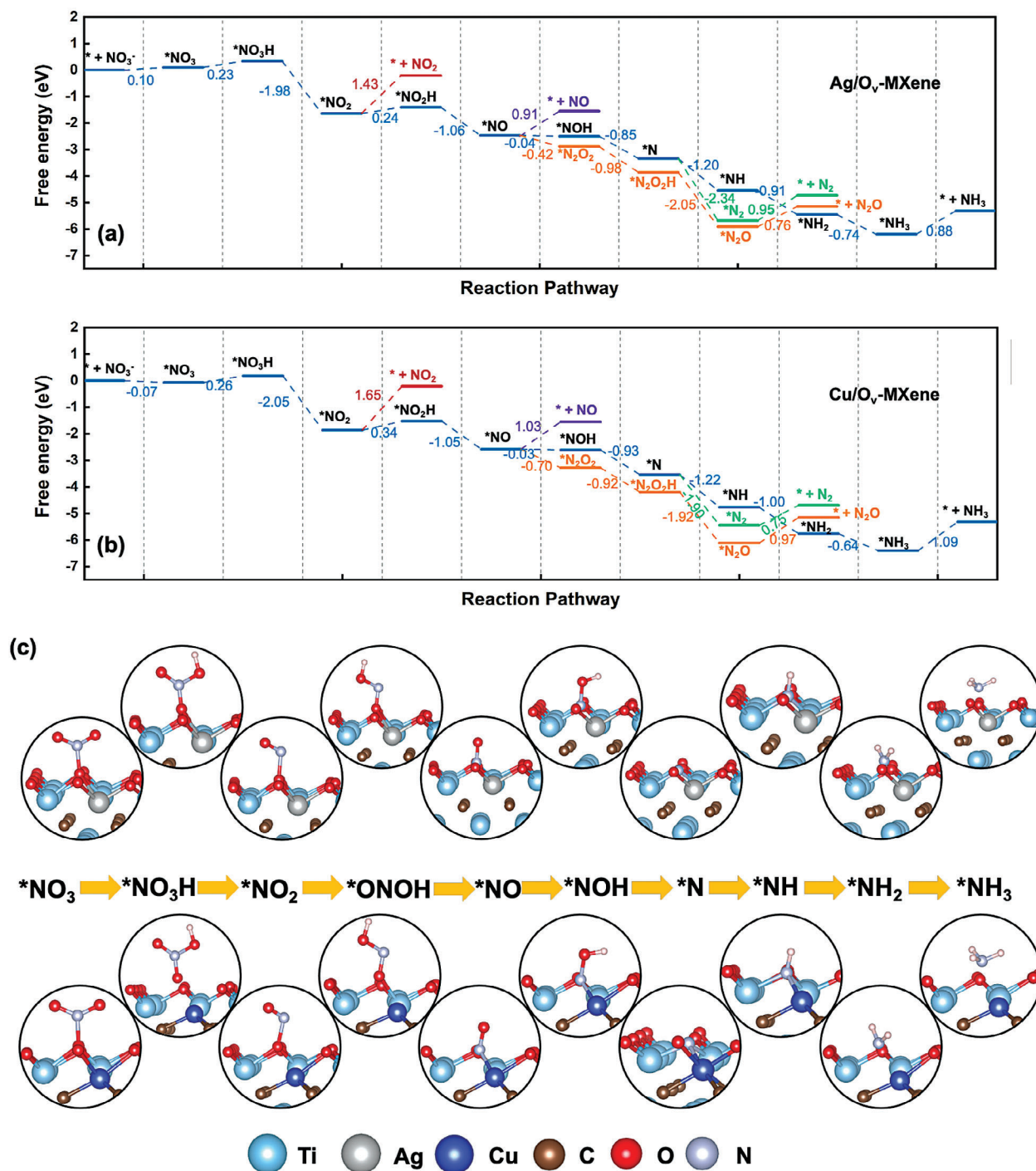
**ADVANCED
SCIENCE NEWS**

www.advancedsciencenews.com

NANO · MICRO
small

www.small-journal.com

Figure 3. a,b) Free energy diagrams (U = 0 V) of NO_3RR on Ag/O_v-MXene and Cu/O_v-MXene, respectively. The pathways to the release of NO_2, NO, N_2, and N_2O are also plotted for comparison. c) Corresponding structures of NO_3RR intermediates adsorbed on Ag/O_v-MXene (above) and Cu/O_v-MXene (below), respectively.

calculated energy barriers of *ON-to-*NO flipping on Ag/O_v-MXene and Cu/O_v-MXene are 0.15 and 0.21 eV, respectively. These results indicate that the switch in binding mode from *ON to *NO is facile. We further construct free energy diagrams of NO_3RR for other TM/O_v-MXene in Figures S10–S12 (Supporting Information) for comparison. During the NO_3RR process, NO_3^-

initially adsorbs onto the catalyst surfaces, generating *NO_3 and *NO_3H intermediates, which subsequently form *NO_2. The reduction of NO_3^- into *NO_2 requires overcoming energy barriers of 0.10, 0.23, and −1.50 eV for Ag/O_v-MXene and −0.07, 0.26, and −2.05 eV for Cu/O_v-MXene, which is in agreement with experimental data.[10] Subsequently, *NO_2 is hydrogenated by (H^+
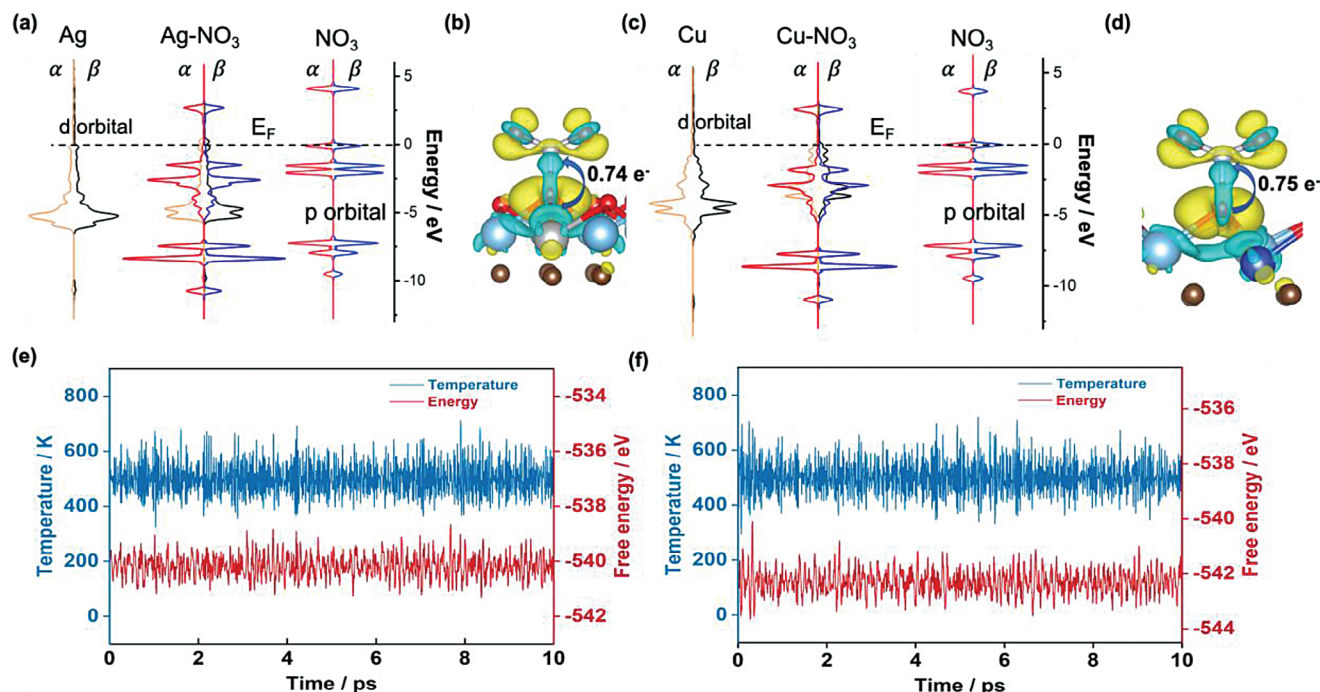
2306311 (5 of 9)

**ADVANCED
SCIENCE NEWS**

www.advancedsciencenews.com

NANO · MICRO

small

www.small-journal.com

Figure 4. a,c) Partial density of states (PDOS) of NO_3^- adsorbed on Ag/O_v-MXene and Cu/O_v-MXene, respectively. E_F denotes the Fermi level, referring to 0 eV. b,d) Charge density differences of NO_3^- adsorbed on Ag/O_v-MXene and Cu/O_v-MXene, respectively. Iso-surfaces are 0.004 eV Å^{-3}. e,f) Energy and temperature evolution versus the AIMD time for Ag/O_v-MXene and Cu/O_v-MXene, respectively. The AIMD simulation in vacuum lasts for 10 ps at 500 K.

+ e$^-$) pair to form $^*NO_2H$ intermediate, which is an endothermic process with an energy difference of 0.24 eV for Ag/O_v-MXene and 0.34 eV for Cu/O_v-MXene. In the following step, $^*NO_2H$ is attacked by a proton to release H_2O, leaving behind $^*NO$ adsorbed on the surface. The changes in the free energy profile are −1.06 and −1.05 eV for Ag/O_v-MXene and Cu/O_v-MXene, respectively. Next, a slightly downhill step from $^*NO$ to $^*NOH$ is observed with the free energy decreased by 0.04 and 0.03 eV for Ag/O_v-MXene and Cu/O_v-MXene, respectively. In the subsequent steps ($^*NOH-^*N-^*NH-^*NH_2-^*NH_3$), the proton consecutively attacks the intermediates, and the corresponding energies drop by 0.85, 1.20, 0.91, and 0.74 eV for Ag/O_v-MXene and 0.93, 1.22, 1.00, and 0.64 eV for Cu/O_v-MXene. Eventually, $^*NH_3$ species are desorbed from the catalyst surface.

To examine the selectivity of NO_3RR toward NH_3, the pathways leading to the formation of byproducts NO_2, NO, N_2O, and N_2 are plotted for comparison in Figure 3a,b. The corresponding structures of these intermediates are shown in Figures S13-S14 (Supporting Information). The energy barriers for the release of NO_2, NO, N_2O, and N_2 on Ag/O_v-MXene reach up to 1.43, 0.91, 0.76, and 0.95 eV, respectively, while on Cu/O_v-MXene they are 1.65, 1.03, 0.97 and 0.75 eV, indicating the difficulty associated to forming these byproducts. In contrast, the desorption of NH_3 requires 0.88 and 1.09 eV for Ag/O_v-MXene and Cu/O_v-MXene, respectively. Notably, NH_3 can be further protonated to NH_4^+ under acidic conditions with a negligible energy barrier as reported in recent studies.[52,53] As shown in Figure 3a,b, $^*NO$ on Ag/O_v-MXene and Cu/O_v-MXene can further react via three distinct paths. The first path is $^*NO$ reduction to form $^*NOH$, the sec-

ond path is NO desorption from the catalyst, and the third path is the coupling of two $^*NO$ to form $^*N_2O_2$. For $^*NO$ reduction into $^*NOH$, this individual step is $^*NO + H^+ + e^- \rightarrow ^*NOH$, which is a proton-coupled electron transfer (PCET) process. The free energy change of this step depends on the applied potential (U). On the other hand, the $^*NO$ desorption and $^*NO$ coupling steps do not involve proton and electron, so the free energy changes of these steps are independent of the applied potential. To visualize the effect of applied potential on the favorability of these three pathways, the free energy diagrams of NO_3RR on Ag/O_v-MXene with $U = -0.38$ V and on Cu/O_v-MXene with $U = -0.67$ V are computed (Figures S15 and S16 (Supporting Information)). The calculated results under applied potential conditions show that the energy change for N_2O_2 formation is the same as the reduction of $^*NO$ into NOH on Ag/O_v-MXene and Cu/O_v-MXene. Therefore, applying potential can alter the NO_3RR selectivity, which is consistent with experiments.[54]

In order to gain insights into the underlying mechanisms behind the high NO_3RR performance of Ag/O_v-MXene and Cu/O_v-MXene, an investigation on the densities of states (DOS) of NO_3^- adsorption on both materials is conducted. Our results indicate that prior to NO_3^- adsorption, the d orbital of Ag and the 2p orbital of NO_3^- lie below the Fermi level, as shown in **Figure 4**a,c. Furthermore, we observed that the energy levels of the d-orbitals of Ag and Cu, as well as the p-orbitals of NO_3^-, are well-matched. Upon NO_3^- adsorption, the d orbital of Ag and Cu mixes with the 2p orbital of NO_3^-, resulting in strong interactions between the transition metal and the adsorbed NO_3^-. To further elucidate the role of charge transfer in dictating

**ADVANCED
SCIENCE NEWS**

www.advancedsciencenews.com

NANO · MICRO

small

www.small-journal.com

the reduction reaction, the charge transfer from the TM atom to NO_3^- is analyzed. Our analysis reveals that there is a charge transfer of 0.74 and 0.75 e^- from the TM SAC to NO_3^- for Ag/O_v-MXene and Cu/O_v-MXene, respectively, which serves as further evidence of the interaction between the TM SAC site and the adsorbed NO_3^-. Additionally, we calculated the PDOS of $^*NO_3$ adsorbed on Cr/O_v-MXene, Au/O_v-MXene, Pd/O_v-MXene, and Pt/O_v-MXene (Figures S17–S20, Supporting Information). The d-band center of Ag, Cu, Cr, Au, Pd, and Pt as well as the corresponding NO_3^- adsorption energy were summarized in Table S3 (Supporting Information). The results show that as the d-band center of transition metal dopant is closer to 0 eV, the energy level of the d-band approaches to that of the p-band of adsorbed NO_3^-. Therefore, Cr, the metal with the highest d-band center (−0.74 eV), displayed the lowest adsorption energy (−0.86 eV). In contrast, Au, the metal with the lowest d-band center (−4.70 eV), showed the highest adsorption energy (0.19 eV). For Ag/O_v-MXene and Cu/O_v-MXene, their moderate d-band centers (−3.34 eV for Ag and −2.62 eV for Cu) resulted in NO_3^- adsorption energies that are neither too strong nor too weak and are optimal to promote efficient NO_3RR. The potential-limiting step of NO_3RR on Ag/O_v-MXene and Cu/O_v-MXene is the reduction of $^*NO_2$ ($^*NO_2 + H^+ + e^- \rightarrow {}^*NO_2H$). To better understand the high NO_3-to-NH_3 reduction activity of Ag/O_v-MXene and Cu/O_v-MXene, we provide the PDOS of $^*NO_2$ and calculate the d-band centers of Ag and Cu and the p-band center of NO_2 (Figures S21 and S22 (Supporting Information)). The calculated results indicate that the d-band center of Ag (−4.02 eV) is significantly different from the p-band center of NO_2 (−1.72 eV), leading to a weak interaction between $^*NO_2$ and the metal active site. In contrast, the d-band center of Cu (−2.59 eV) is closer to the p-band center of NO_2 (−1.78 eV), leading to a strong interaction between the Cu active site and the adsorbed NO_2. This strong interaction leads to favorable $^*NO_2$ adsorption but also increases the energy penalty for the subsequent reduction step of $^*NO_2$. As shown in Figure 3a,b, the free energy change of the reduction of $^*NO_2$ is 0.24 eV on Ag/O_v-MXene, which is lower than that on Cu/O_v-MXene (0.34 eV). These results are consistent with the PDOS analysis.

2.4. Stability of Ag/O$_v$-Mxene and Cu/O$_v$-Mxene

To evaluate the thermodynamic stability of TM/O_v-MXene, we calculate the formation energy (E_{form}) for each candidate (details described in the Experimental Section). All the E_{form} of the oxygen vacancy MXene-based SACs are summarized in Figure S23 (Supporting Information). For Ag/O_v-MXene and Cu/O_v-MXene, the computed E_{form} values are +2.30 and +2.41 eV, respectively. Previously, oxygen-defective MXene embedded with a single atom has been prepared experimentally,[47] and the computed E_{form} of Pt_{SA} doped on oxygen-defective $Mo_2TiC_2O_2$ is +2.62 eV.[55] Taken together, the lower formation energy of Ag/O_v-MXene and Cu/O_v-MXene relative to the Pt case corroborates that Ag/O_v-MXene and Cu/O_v-MXene should be thermodynamically stable. To further investigate the stability of the catalysts, we performed ab initio molecular dynamics (AIMD) simulations at 500 K for Ag/O_v-MXene and Cu/O_v-MXene in a vacuum. As shown in Figure 4e,f, the total energy oscillates near the initial condition, and the ge-

ometric structures of Ag/O_v-MXene and Cu/O_v-MXene remain well-preserved during the 10 ps simulation. To evaluate the stability of TM/O_v-MXene in water, an explicit model with H_2O molecules added on top of the catalyst surface of interest was applied for AIMD simulation at 500 K. The simulated models were shown in Figure S24 (Supporting Information), and the energy changes were displayed in Figure S25 (Supporting Information). These results indicate that the catalysts are sufficiently stable, further supporting that their structures can be maintained in the presence of H_2O. These results lead to the conclusion that Ag/O_v-MXene and Cu/O_v-MXene can serve as highly efficient and stable catalysts for selective ammonia synthesis through electrochemical NO_3RR.

3. Conclusion

In this work, we utilized density functional theory (DFT) calculations to investigate the potential application of SACs supported on defective $Ti_3C_2O_2$ nanosheets with oxygen vacancies for electrocatalytic NO_3RR to produce NH_3. By employing the scaling relationship and contour plot, our computations demonstrated that Ag/O_v-MXene (for precious metal) and Cu/O_v-MXene (for non-precious metal) exhibit outstanding low limiting potentials for NO_3RR of −0.24 and −0.34 V, respectively. Additionally, the adsorption energy of NO_3^- on Ag/O_v-MXene and Cu/O_v-MXene is stronger than that of the proton, which favors NO_3RR and suppresses the HER. With respect to selectivity, high energy barriers for the release of NO_2, NO, N_2O, and N_2 on Ag/O_v-MXene and Cu/O_v-MXene facilitate the production of ammonia. The density of state and charge density difference analysis provide insights into the superior NO_3RR performance on Ag/O_v-MXene and Cu/O_v-MXene. The stability of Ag/O_v-MXene and Cu/O_v-MXene is verified through formation energy and ab initio molecular dynamics (AIMD) simulations at 500 K. Our theoretical study suggests that Ag/O_v-MXene and Cu/O_v-MXene are highly active, selective, and robust electrocatalysts for NO_3RR to produce ammonia under ambient conditions.

4. Experimental Section

Spin-polarized DFT calculations were conducted to optimize the atomic positions of the structures by VASP[56] using the projector augmented wave (PAW) potentials with a plane-wave cutoff energy of 450 eV.[57,58] The generalized gradient approximation (GGA) functional of Perdew, Burke, and Ernzerhof (PBE) was applied as the exchange-correlation functional.[59] All structures were fully optimized until achieving the convergence criteria of 10^{-5} eV for electronic energies and 0.03 eV Å^{-1} for atomic forces. The grimme's semi-empirical DFT-D3 dispersion correction was utilized to describe the van der Waals (vdW) interactions.[60] The $3 \times 3 \times 1$ supercell of $Ti_3C_2O_2$ was used to model defective MXenes as SAC-supporting substrates. In order to eliminate the effects between two adjacent layers, a vacuum region of 15 Å was added in the z-direction. For structural optimizations, the Brillouin zones integrations were performed with a gamma-centered $3 \times 3 \times 1$ Monkhorst-Pack k-point mesh grid, whereas k-point mesh was increased to $5 \times 5 \times 1$ for the density of states (DOS) calculations. The CI-NEB method as implemented in VTST tools was applied to calculate the transition states with a convergence criterion of 0.05 eV Å^{-1} for atomic forces.[61] The solvation effect was not included since it has little effect on energy variation.[52,62] Bader charge population analysis was applied to describe the charge variation of the intermediates in the NO_3RR process.[63] To evaluate the thermal stability of

the catalysts, AIMD simulations were performed both in a vacuum and using an explicit model (with 20 H_2O molecules added on the top of the catalyst surface) in the NVT canonical ensemble at 500 K for 10 ps, using a time step of 1 fs.[64] VASPKIT, as a postprocessing program for the VASP code, was adopted to analyze the DOS diagrams and charge density difference.[65]

The Gibbs free energy calculations for NO_3RR were based on the computational hydrogen electrode (CHE) model.[66] The free energy of the proton-coupled electron pair of ($H^+ + e^-$) is related to that of 1/2 $H_{2(g)}$. The change of Gibbs free (ΔG) of each individual step during the NO_3RR process was calculated by:

$$\Delta G = \Delta E + \Delta ZPE - T\Delta S + Ue + \Delta G_{pH} \quad (1)$$

where ΔE is the DFT calculated reaction energy difference between the reactants and the products, ΔZPE is the zero-point energy, ΔS is the entropy change (summarized in Table S4, Supporting Information), T represents the finite temperature, e is the charge transferred, U is the applied potential, and ΔG_{pH} is considered as the correction free energy of H^+.

The Gibbs free energy change of charged $NO_3^-{}_{(aq)}$ adsorbed on the electrode surface was calculated by a thermodynamic cycle (see Supporting Information for details), the expression is described as:

$$\Delta G_{*NO3} = G_{*NO3} - G_{sur} - G_{HNO3(g)} + 1/2G_{H2(g)} + \Delta G_{correct} \quad (2)$$

where G_{*NO3}, G_{sur}, $G_{HNO3(g)}$, and $G_{H2(g)}$ are the Gibbs free energy of NO_3^- adsorbed on TM/O_v-MXenes, O_v-MXenes, HNO_3, and H_2 gas molecule. $\Delta G_{correct}$ denotes the correction of adsorption energy and was set to 0.392 eV.

The formation energy of TM/O_v-MXene is described as:

$$\Delta E_{form} = E_{TM/MXene} + E_{Ti} - E_{MXene} - E_{TM} - \frac{1}{2} E_{O2(g)} \quad (3)$$

where $E_{TM/MXene}$ and E_{MXene} are the energy of $Ti_3C_2O_2$ after and before the single transition metal atom immobilization; while E_{Ti}, E_{TM}, and E_{O2} are the per atom energy of the bulk unit cell of Ti, the embedded single transition metal atom, and an O_2 gas molecule, respectively.

Supporting Information

Supporting Information is available from the Wiley Online Library or from the author.

Conflict of Interest

The authors declare no conflict of interest.

Data Availability Statement

The data that support the findings of this study are available from the corresponding author upon reasonable request.

[1] N. Gruber, J. N. Galloway, *Nature* **2008**, *451*, 293.

[2] D. E. Canfield, A. N. Glazer, P. G. Falkowski, *Science* **2010**, *330*, 192.

[3] J. G. Chen, R. M. Crooks, L. C. Seefeldt, K. L. Bren, R. M. Bullock, M. Y. Darensbourg, P. L. Holland, B. Hoffman, M. J. Janik, A. K. Jones, M. G. Kanatzidis, P. King, K. M. Lancaster, S. V. Lymar, P. Pfromm, W. F. Schneider, R. R. Schrock, *Science* **2018**, *360*, eaar6611.

[4] J. J. Schoeman, A. Steyn, *Desalination* **2003**, *155*, 15.

[5] A. M. Bergquist, J. K. Choe, T. J. Strathmann, C. J. Werth, *Water Res.* **2016**, *96*, 177.

[6] S. G. Lehman, M. Badruzzaman, S. Adham, D. J. Roberts, D. A. Clifford, *Water Res.* **2008**, *42*, 969.

[7] D. P. Butcher, A. A. Gewirth, *Nano Energy* **2016**, *29*, 457.

[8] S. Ghafari, M. Hasan, M. K. Aroua, *Bioresour. Technol.* **2008**, *99*, 3965.

[9] W. Wang, E. C. M. Tse, *Eur. J. Inorg. Chem.* **2022**, *2022*, e202200291.

[10] G. E. Dima, A. C. A. De Vooys, M. T. M. Koper, *J. Electroanal. Chem.* **2003**, *554–555*, 15.

[11] K. Shimazu, R. Goto, S. Piao, R. Kayama, K. Nakata, Y. Yoshinaga, *J. Electroanal. Chem.* **2007**, *601*, 161.

[12] W. Siriwatcharapiboon, Y. Kwon, J. Yang, R. L. Chantry, Z. Li, S. L. Horswell, M. T. M. Koper, *ChemElectroChem* **2014**, *1*, 172.

[13] Y. Wang, A. Xu, Z. Wang, L. Huang, J. Li, F. Li, J. Wicks, M. Luo, D.-H. Nam, C.-S. Tan, Y. Ding, J. Wu, Y. Lum, C.-T. Dinh, D. Sinton, G. Zheng, E. H. Sargent, *J. Am. Chem. Soc.* **2020**, *142*, 5702.

[14] R. Jia, Y. Wang, C. Wang, Y. Ling, Y. Yu, B. Zhang, *ACS Catal.* **2020**, *10*, 3533.

[15] Y. Wang, W. Zhou, R. Jia, Y. Yu, B. Zhang, *Angew. Chem., Int. Ed.* **2020**, *59*, 5350.

[16] S. Li, J. Liang, P. Wei, Q. Liu, L. Xie, Y. Luo, X. Sun, *eScience.* **2022**, *2*, 382.

[17] J. Zhao, Z. Chen, *J. Am. Chem. Soc.* **2017**, *139*, 12480.

[18] H. Zhang, G. Liu, L. Shi, J. Ye, *Adv. Energy Mater.* **2018**, *8*, 1701343.

[19] C. Zhu, S. Fu, Q. Shi, D. Du, Y. Lin, *Angew. Chem., Int. Ed.* **2017**, *56*, 13944.

[20] J. Su, R. Ge, Y. Dong, F. Hao, L. Chen, *J. Mater. Chem. A* **2018**, *6*, 14025.

[21] Y. Da, R. Jiang, Z. Tian, X. Han, W. Chen, W. Hu, *SmartMat* **2023**, *4*, e1136.

[22] B. Qiao, A. Wang, X. Yang, L. F. Allard, Z. Jiang, Y. Cui, J. Liu, J. Li, T. Zhang, *Nat. Chem.* **2011**, *3*, 634.

[23] H. Fei, J. Dong, M. J. Arellano-Jiménez, G. Ye, N. D. Kim, E. L. G. Samuel, Z. Peng, Z. Zhu, F. Qin, J. Bao, M. J. Yacaman, P. M. Ajayan, D. Chen, J. M. Tour, *Nat. Commun.* **2015**, *6*, 8668.

[24] J. Liu, M. Jiao, L. Lu, H. M. Barkholtz, Y. Li, Y. Wang, Z. Wu, D. J. Liu, L. Zhuang, C. Ma, J. Zeng, B. Zhang, D. Su, P. Song, W. Xing, W. Xu, Y. Wang, Z. Jiang, G. Sun, *Nat. Commun.* **2017**, *8*, 15938.

[25] H. Fei, J. Dong, Y. Feng, C. S. Allen, C. Wan, B. Volosskiy, M. Li, Z. Zhao, Y. Wang, H. Sun, P. An, W. Chen, Z. Guo, C. Lee, D. Chen, I.

**ADVANCED
SCIENCE NEWS**

www.advancedsciencenews.com

NANO · MICRO

small

www.small-journal.com

Shakir, M. Liu, T. Hu, Y. Li, A. I. Kirkland, X. Duan, Y.u Huang, *Nat. Catal.* **2018**, *1*, 63.

[26] Y. Pan, R. Lin, Y. Chen, S. Liu, W. Zhu, X. Cao, W. Chen, K. Wu, W.-C. Cheong, Y. Wang, L. Zheng, J. Luo, Y. Lin, Y. Liu, C. Liu, J. Li, Q. Lu, X. Chen, D. Wang, Q. Peng, C. Chen, Y. Li, *J. Am. Chem. Soc.* **2018**, *140*, 4218.

[27] J. Li, S. Chen, F. Quan, G. Zhan, F. Jia, Z. Ai, L. Zhang, *Chem* **2020**, *6*, 885.

[28] S. Tang, T. Liu, Q. Dang, X. Zhou, X. Li, T. Yang, Y. Luo, E. Sharman, J. Jiang, *J. Phys. Chem. Lett.* **2020**, *11*, 5051.

[29] N. Li, Z. Wang, P. Zhang, X. Li, A. Arramel, C. Sun, X. Zhou, X. Zhao, *J. Mater. Chem. A* **2022**, *10*, 22760.

[30] X. Chen, X. Zhao, Z. Kong, W.-J. Ong, N. Li, *J. Mater. Chem. A* **2018**, *6*, 21941.

[31] Y. Yang, J. Peng, Z. Shi, P. Zhang, A. Arramel, N. Li, *J. Mater. Chem. A* **2023**, *11*, 6428.

[32] H. Niu, Z. Zhang, X. Wang, X. Wan, C. Shao, Y. Guo, *Adv. Funct. Mater.* **2021**, *31*, 2008533.

[33] F. Rehman, S. Kwon, C. B. Musgrave, M. Tamtaji, W. A. Goddard, Z. Luo, *Nano Energy* **2022**, *103*, 107866.

[34] B. Anasori, M. R. Lukatskaya, Y. Gogotsi, *Nat. Rev. Mater.* **2017**, *2*, 16098.

[35] M. Naguib, V. N. Mochalin, M. W. Barsoum, Y. Gogotsi, *Adv. Mater.* **2014**, *26*, 992.

[36] Y. Wang, Y. Wang, *SmartMat* **2023**, *4*, e1130.

[37] C. Ling, L. Shi, Y. Ouyang, J. Wang, *Chem. Mater.* **2016**, *28*, 9026.

[38] C. Ling, L. Shi, Y. Ouyang, Q. Chen, J. Wang, *Adv. Sci.* **2016**, *3*, 1600180.

[39] Y. Gao, Y. Cao, H. Zhuo, X. Sun, Y. Gu, G. Zhuang, S. Deng, X. Zhong, Z. Wei, X. Li, J.-G. Wang, *Catal. Today* **2020**, *339*, 120.

[40] L. M. Azofra, N. Li, D. R. Macfarlane, C. Sun, *Energy Environ. Sci.* **2016**, *9*, 2545.

[41] Y. Luo, G.-F. Chen, L. Ding, X. Chen, L.-X. Ding, H. Wang, *Joule* **2019**, *3*, 279.

[42] B. Huang, N. Li, W.-J. Ong, N. Zhou, *J. Mater. Chem. A* **2019**, *7*, 27620.

[43] A. D. Handoko, K. H. Khoo, T. L. Tan, H. Jin, Z. W. Seh, *J. Mater. Chem. A* **2018**, *6*, 21885.

[44] N. Li, X. Chen, W.-J. Ong, D. R. Macfarlane, X. Zhao, A. K. Cheetham, C. Sun, *ACS Nano* **2017**, *11*, 10825.

[45] N. Li, X. Wang, X. Lu, P. Zhang, W.-J. Ong, *Chem. – A Eur. J.* **2021**, *27*, 17900.

[46] E. C. M. Tse, C. J. Barile, N. A. Kirchschlager, Y. Li, J. P. Gewargis, S. C. Zimmerman, A. Hosseini, A. A. Gewirth, *Nat. Mater.* **2016**, *15*, 754.

[47] J. Zhang, Y. Zhao, X. Guo, C. Chen, C.-L. Dong, R.-S. Liu, C.-P. Han, Y. Li, Y. Gogotsi, G. Wang, *Nat. Catal.* **2018**, *1*, 985.

[48] D. Zhao, Z. Chen, W. Yang, S. Liu, X. Zhang, Y. Yu, W.-C. Cheong, L. Zheng, F. Ren, G. Ying, X. Cao, D. Wang, Q. Peng, G. Wang, C. Chen, *J. Am. Chem. Soc.* **2019**, *141*, 4086.

[49] L. Li, X. Wang, H. Guo, G. Yao, H. Yu, Z. Tian, B. Li, L. Chen, *Small Methods* **2019**, *3*, 1900337.

[50] M. Naguib, M. Kurtoglu, V. Presser, J. Lu, J. Niu, M. Heon, L. Hultman, Y. Gogotsi, M. W. Barsoum, *Adv. Mater.* **2011**, *23*, 4248.

[51] S. Garcia-Segura, M. Lanzarini-Lopes, K. Hristovski, P. Westerhoff, *Appl Catal B* **2018**, *236*, 546.

[52] X. Guo, J. Gu, S. Lin, S. Zhang, Z. Chen, S. Huang, *J. Am. Chem. Soc.* **2020**, *142*, 5709.

[53] I. Katsounaros, M. C. Figueiredo, X. Chen, F. Calle-Vallejo, M. T. M. Koper, *ACS Catal.* **2017**, *7*, 4660.

[54] J. F. Su, I. Ruzybayev, I. Shah, C. P. Huang, *Appl Catal B* **2016**, *180*, 199.

[55] N. Li, W. J. Ong, M. Yao, Z. Shi, P. Zhang, J. Jiang, W. Y. Ching, *ACS Appl. Nano Mater.* **2020**, *3*, 9870.

[56] G. Kresse, J. Furthmüller, *Phys Rev B Condens Matter Mater Phys* **1996**, *54*, 11169.

[57] P. E. Blöchl, *Phys. Rev. B* **1994**, *50*, 17953.

[58] D. Joubert, *Phys Rev B Condens. Matter Mater. Phys.* **1999**, *59*, 1758.

[59] J. P. Perdew, K. Burke, M. Ernzerhof, *Phys. Rev. Lett.* **1996**, *77*, 3865.

[60] S. Grimme, J. Antony, S. Ehrlich, H. Krieg, *J. Chem. Phys.* **2010**, *132*, 154104.

[61] G. Henkelman, B. P. Uberuaga, H. Jónsson, *J. Chem. Phys.* **2000**, *113*, 9901.

[62] J. H. Montoya, C. Tsai, A. Vojvodic, J. K. Nørskov, *ChemSusChem* **2015**, *8*, 2180.

[63] W. Tang, E. Sanville, G. Henkelman, *J Phys Condens Matter* 084204, **2009**, *21*,.

[64] S. Nosé, *J. Chem. Phys.* **1984**, *81*, 511.

[65] V. Wang, N. Xu, J.-C. Liu, G. Tang, W.-T. Geng, *Comput. Phys. Commun.* **2021**, *267*, 108033.

[66] J. K. Nørskov, J. Rossmeisl, A. Logadottir, L. Lindqvist, J. R. Kitchin, T. Bligaard, H. Jónsson, *J. Phys. Chem. B* **2004**, *108*, 17886.